Advances in Applied Mathematics and Mechanics
Adv. Appl. Math. Mech., Vol. **3**, No. 6, pp. 702-715

DOI: 10.4208/aamm.11-m1109
December 2011

Mathematical Simulation of Metamaterial Solar Cells

Jichun Li[1,2,*], Yitung Chen[3] and Yang Liu[3]

[1] *Hunan Key Laboratory for Computation and Simulation in Science and Engineering, Xiangtan University, Hunan 411105, China*
[2] *Department of Mathematical Sciences, University of Nevada Las Vegas, Las Vegas, Nevada 89154-4020, USA*
[3] *Department of Mechanical Engineering, University of Nevada Las Vegas, Las Vegas, Nevada 89154-4027, USA*

Received 24 December 2010; Accepted (in revised version) 17 May 2011

Available online 31 October 2011

Abstract. In this paper, we propose several solar cell designs based on metamaterials. Extensive numerical simulations of various designs with different materials are carried out. Our tests show that metamaterial solar cells are quite efficient, and over 80% and 90% absorption rates can be attained for solar spectrum and visible rays, respectively.

AMS subject classifications: 78M10, 65N30, 35L15

Key words: Maxwell's equations, metamaterial, solar cell, finite element method.

1 Introduction

A solar cell is a device that converts the sunlight energy directly into electricity through the photovoltaic effect. The high-efficient solar cell is a class of solar cells that can generate more electricity per incident solar power. Much of the industry is focused on the most cost efficient technologies in terms of cost per generated power. The two main strategies to bring down the cost of photovoltaic electricity are either by increasing the efficiency of the cells or by decreasing their cost per unit area. The challenge of increasing the photovoltaic efficiency is thus of great interest, both from the academic and economic points of view.

The Sun is a sphere of intensely hot gaseous matter with a diameter of 1.39×10^9 meters (m) and is, on the average, 1.5×10^{11}m from the Earth. The Sun has an effective black body temperature 5777 kelvins. Many solar cells are designed to absorb a wavelength range of 0.25 to 3.0 micron, the portion of the electromagnetic radiation

*Corresponding author.
URL: `http://faculty.unlv.edu/jichun/`
Email: jichun@unlv.nevada.edu (J. Li), uuchen@nscee.edu (Y. Chen), yang.liu2009@hotmail.com (Y. Liu)

that includes most of the energy radiated by the Sun. The solar cell has been continuously developed for more than four decades. The traditional energy conversion is from chemical energy to mechanical energy and then to electrical energy. The burning or heating process is used to convert chemical energy to mechanical energy. The steam power thermodynamics cycle is used to drive high pressure steam turbines to connect the generator to generate electricity. The total efficiency of generating electricity using the traditional technology is low, since the total efficiency is equal to the product of all process efficiencies. A solar cell can directly convert radiation energy to electrical energy which is more desirable compared to the traditional energy conversion technology because of zero emission of NO_2, CO_2 and SO_2 that are usually found from coal or natural gas combustion process. In addition, the traditional coal or gas-fired power plant is not sustainable. The major disadvantage of using solar cell to generate electricity is high cost and low efficiency. It is because the current solar cell technology is still silicon-based.

Generally speaking, solar cells can be classified into six categories: (1) monocrystalline silicon solar cells, (2) polycrystalline silicon solar cells, (3) polysilicon thin film solar cells, (4) amorphous silicon solar cells, (5) amorphous silicon thin film solar cells, and (6) multi-component solar cells. The most common single-crystal silicon cells are used for power plants, charging systems, lighting and traffic signals, and so on. The world's leading solar cell manufacturers such as Siemens in Germany, United Kingdom Oil in U.K. and Sharp in Japan have produced the single-crystal silicon-based solar cells with efficiency from 11% to 24%. Though polysilicon cells are less expensive to produce than single crystal silicon cells, they are less efficient. Various thin-film technologies have been developed to reduce the amount of material used in making solar cells. It can reduce the processing costs from using less bulk materials, but it tends to reduce the energy conversion efficiency in a range of 7% to 10%. It is known that the efficiency can be improved by using many multi-layer thin films. The thin film solar cells become more popular compared to wafer silicon technology because of high flexibility, low weight, and easy system integration. The multi-junction process has been developed to absorb most solar spectrum to improve the solar cell efficiency. But the high cost is still a big concern of using multi-junction process.

In this paper we will investigate a complete different approach on the solar cell design, which is based on the use of electromagnetic metamaterials to increase solar cell efficiency. Electromagnetic metamaterials are artificially structured media with unique and exotic properties that are not observed in natural materials. In 1968, Veselago [10] published a seminar paper addressing what would happen if the permittivity and permeability of a material are simultaneously negative rather than positive for most natural electromagnetic materials. He found that the results would be very interesting and exotic: one would find backward waves in metamaterials, and the refractive index of the metamaterial is negative. Unfortunately, materials with simultaneously negative permittivity and permeability do not exist in nature. For this reason, no further progress was made along this direction until 2000, when David Smith et al. [8] successfully constructed such an artificially structured composite material. Since 2000,

the field of electromagnetic metamaterials has been rapidly developed. In the past 10 years, both two and three dimensional metamaterials have been realized in practice, the scaling of these artificial structures has been demonstrated from radio frequencies to microwaves, terahertz, far infrared, and near infrared wavelengths, spanning nearly seven orders of magnitude in frequency. One of the most striking properties is the so-called re-focusing property: in a planar negative-index slab, an evanescent wave decaying away from an object grows exponentially in the slab; on exiting the negative-index slab, the wave decays again (see Fig. 1 of our paper [6]). This property shows that metamaterials hold a great promise in becoming efficient subwavelength absorbers [1]. Ultra-thin slabs of such metamaterials have been shown [2] to sustain their high absorptivity for a wide range of incident angles. The resulting wide-angle ultra-thin absorber is highly desirable for developing efficient thermalphotovoltaics (TPV) [5, 9] and photovoltaics (PV) [3]. In photovoltaic applications, the efficiency of solar cells can be enhanced by the strong field resonance inside the absorbing metamaterial.

The rest of the paper is organized as follows. In Section 2, we present the governing equations for our solar cell simulation. In Section 3, we present our tests for many different solar cell designs. We conclude the paper in Section 4.

2 The mathematical formulation

Modeling of electromagnetic phenomena is governed by the Maxwell's equations:

$$\nabla \times \widetilde{\boldsymbol{H}} = \frac{\partial \widetilde{\boldsymbol{D}}}{\partial t}, \tag{2.1a}$$

$$\nabla \times \widetilde{\boldsymbol{E}} = -\frac{\partial \widetilde{\boldsymbol{B}}}{\partial t}, \tag{2.1b}$$

where $\widetilde{\boldsymbol{E}}(\boldsymbol{x},t)$ and $\widetilde{\boldsymbol{H}}(\boldsymbol{x},t)$ are the electric and magnetic fields, and $\widetilde{\boldsymbol{D}}(\boldsymbol{x},t)$ and $\widetilde{\boldsymbol{B}}(\boldsymbol{x},t)$ are the corresponding electric and magnetic flux densities. For linear materials, we have the constitutive relations

$$\widetilde{\boldsymbol{D}} = \epsilon_0\epsilon_r\widetilde{\boldsymbol{E}}, \qquad \widetilde{\boldsymbol{B}} = \mu_0\mu_r\widetilde{\boldsymbol{H}}, \tag{2.2}$$

where ϵ_0 and μ_0 are the free space permittivity and permeability, and ϵ_r and μ_r are the relative permittivity and permeability.

Assuming the time harmonic form

$$\widetilde{\boldsymbol{E}}(\boldsymbol{x},t) = \boldsymbol{E}(\boldsymbol{x})e^{j\omega t}, \qquad \widetilde{\boldsymbol{H}}(\boldsymbol{x},t) = \boldsymbol{H}(\boldsymbol{x})e^{j\omega t},$$

where ω denotes the wave frequency, then substituting (2.2) into (2.1a)-(2.1b), we have

$$j\omega\epsilon_0\epsilon_r\boldsymbol{E} = \nabla \times \boldsymbol{H}, \tag{2.3a}$$

$$j\omega\mu_0\mu_r\boldsymbol{H} = -\nabla \times \boldsymbol{E}. \tag{2.3b}$$

From (2.3a)-(2.3b), we can combine these two equations into an equation for either the electric field or the magnetic field:

$$\nabla \times (\mu_r^{-1} \nabla \times \boldsymbol{E}) - k_0^2 \epsilon_r \boldsymbol{E} = 0, \tag{2.4a}$$

$$\nabla \times (\epsilon_r^{-1} \nabla \times \boldsymbol{H}) - k_0^2 \mu_r \boldsymbol{H} = 0, \tag{2.4b}$$

where k_0 denotes the wave number of free space $k_0 = \omega\sqrt{\epsilon_0 \mu_0} = \omega/c_0$, where c_0 is the speed of light in free space.

Assuming that the material is non-magnetic (i.e., $\mu_r = 1$), then we can use the refractive index n to rewrite (2.4a)-(2.4b) as

$$\nabla \times (\nabla \times \boldsymbol{E}) - k_0^2 n^2 \boldsymbol{E} = 0, \tag{2.5a}$$

$$\nabla \times (n^{-2} \nabla \times \boldsymbol{H}) - k_0^2 \boldsymbol{H} = 0, \tag{2.5b}$$

where $n^2 = \epsilon_r \mu_r$.

Our implementation is based on COMSOL Multiphysics package. For efficient modeling, our simulation is for 2-D transverse electric modeling: we first solve Eq. (2.5b) for the scalar unknown $H = H_z$ by using the lowest-order triangular edge element basis function, then postprocess H by using (2.3a) to obtain unknowns

$$\boldsymbol{E} = (E_x, E_y)',$$

i.e.,

$$E_x = \frac{1}{j\omega\epsilon_0\epsilon_r}\frac{\partial H}{\partial y}, \qquad E_y = \frac{-1}{j\omega\epsilon_0\epsilon_r}\frac{\partial H}{\partial x}.$$

3 Numerical results

3.1 A benchmark problem

We first test a benchmark problem proposed by Wu et al. [11]. The proposed geometric structure for the solar cell is illustrated in Fig. 1. The structure is uniform in the z-

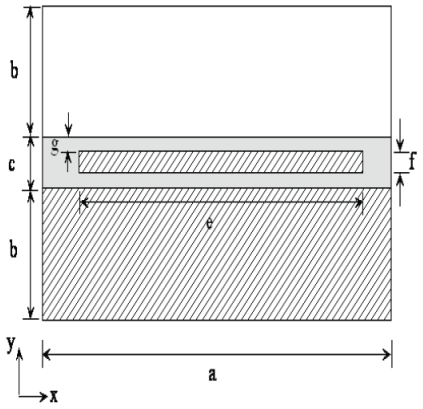

Figure 1: The unit cell structure for the benchmark problem.

direction and the unit cell has periodic boundary conditions in the x-direction. The unit cell contains a benzocyclobutene (BCB) layer with thickness $c = 5 \times 10^{-8}$m, and a substrate made of gold with thickness $b = 1 \times 10^{-7}$m. The gold substrate is used to absorb the radiation energy coming into the cell. There is a gold strip embedded inside the BCB layer with dimension $f \times e$, while g denotes the gap between the strip and the BCB boundary. The parameters f, e and g can be adjusted to get a good absorption

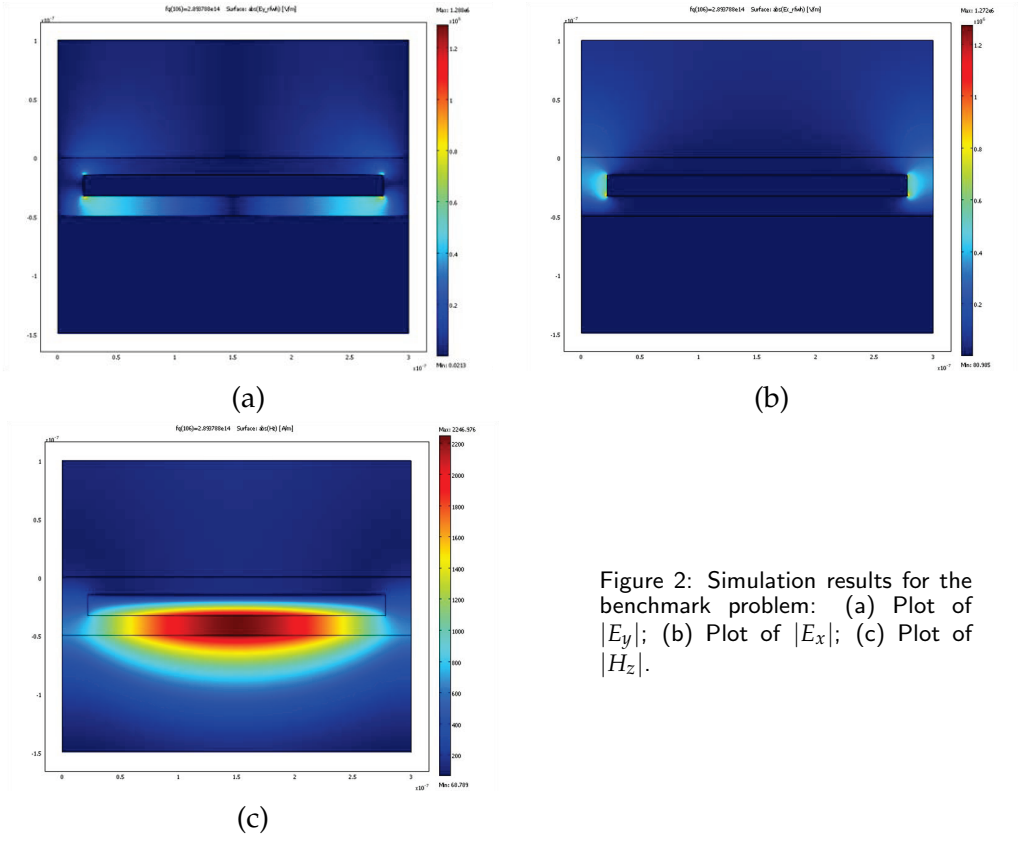

Figure 2: Simulation results for the benchmark problem: (a) Plot of $|E_y|$; (b) Plot of $|E_x|$; (c) Plot of $|H_z|$.

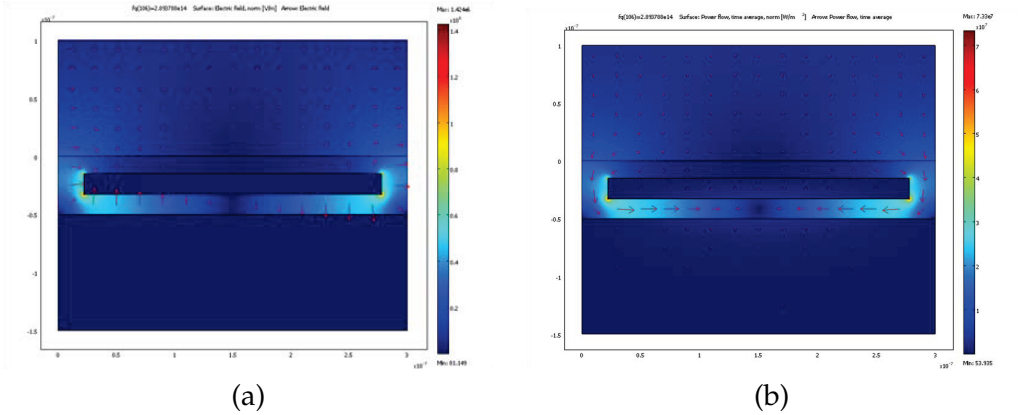

Figure 3: The benchmark problem: (a) Plot of the electric field; (b) Plot of power flow.

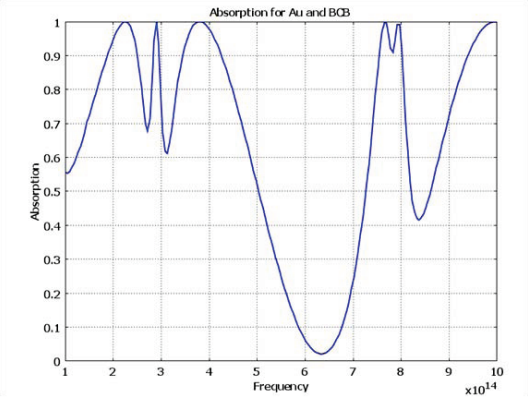

Figure 4: The benchmark problem: The absorption corresponding to the infrared and visible frequencies with zero incident angle.

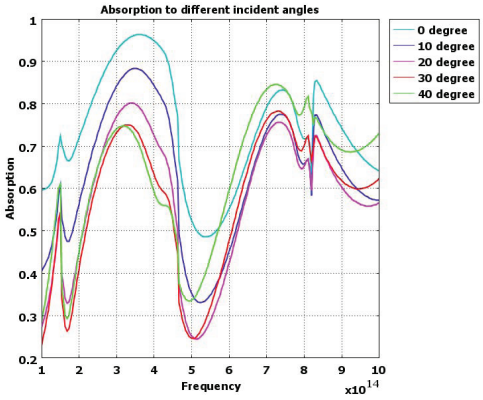

Figure 5: The benchmark problem: The absorption corresponding to the infrared and visible frequencies with various incident angles.

for the solar cell. Here we choose $g = 1.5 \times 10^{-8}$m, $f = 1.8 \times 10^{-8}$m and $e = 2.56 \times 10^{-7}$m, since our tests showed that sometimes the attained cell absorption rate can be more than 90% for an electromagnetic radiation in the infrared and ultraviolet regions.

The permittivity for gold is modeled by the Drude model [4,7]

$$\epsilon_g(\omega) = 1 - \frac{\omega_p^2}{\omega(\omega + i\gamma)},$$

where the effective plasma frequency ω_p and the collision frequency γ are calculated as

$$\gamma = \frac{\omega\epsilon_2}{1-\epsilon_1}, \qquad \omega_p = \sqrt{(1-\epsilon_1)(\omega^2+\gamma^2)},$$

where ϵ_1 and ϵ_2 are functions of the incident wavelength λ, obtained through polynomial fitting. More specifically, we have

$$\epsilon_1 = -1.1\lambda^3 - 39\lambda^2 - 12\lambda + 12,$$
$$\epsilon_2 = 7.3\lambda^8 - 100\lambda^7 + 580\lambda^6 - 1900\lambda^5 + 3700\lambda^4 - 4400\lambda^3 + 3200\lambda^2 - 1300\lambda + 210.$$

In simulation, we choose the refractive index $n = 1.56$ for BCB, and adopt the port condition at both incident and exit surfaces. Furthermore, Floquet periodic boundary condition is used in the x-direction. At interfaces between subdomains, we impose the tangential continuity condition.

In our simulation, the absorption on a fixed port is defined as $1 - |S_{11}|^2$, where S_{11} is the reflection coefficient, which in terms of the power flow is expressed as

$$S_{11} = \frac{\sqrt{\text{Power reflected from the port}}}{\sqrt{\text{Power incident on the port}}}.$$

For a P-polarized radiation at frequency 2.89×10^{14}Hz (which is in the infrared region) with zero degree incident angle (i.e., penetrating the solar cell vertically), the obtained electric and magnetic field magnitudes $|E_x|$, $|E_y|$ and $|H_z|$ are plotted in Fig. 2, which is similar to those obtained by Wu et al. [11].

In Fig. 3, we plot the electric field and the power flow, which clearly shows that the radiation is absorbed by the gold and BCB material with very little reflection.

Then we plot the absorption corresponding to the infrared (IR) and visible frequencies in Fig. 4, which shows that the absorption is over 60% for most frequencies in the IR and visible region.

Finally, we carried out many numerical experiments by varying the incident angles. Fig. 5 shows how the absorption varies with the incident angles for the IR and visible region. Generally speaking, the absorption decreases as the incident angle increases for fixed frequencies. Our results show that the average absorption is about 60% for all incident angles between 0 and 40 degrees.

3.2 Tests of other materials

The solar spectrum picture (see Fig. 6) shows that strong radiation energy happens at the visible region, so the absorption peak is expected to happen in this region: i.e., with frequency ranging from 4.0×10^{14}Hz to 7.5×10^{14}Hz. Considering the expensive cost of gold and the uncommon BCB material, we tested three different materials for their absorptions in order to find a cheap but efficient solar cell design. On one hand, we replace the expensive gold by metals with high absorption and high melting temperature such as Cu, Ni, and tungsten denoted as W. On the other hand, we replace BCB by dielectric SiO_2, semiconductor C[100] and Poly-Si, respectively.

In our tests, we choose refractive indices 1.483, 1.457, 3.882 for SiO_2, semiconductor C[100] and Poly-Si, respectively. The permittivity for Cu, Ni, and tungsten is still modeled by the Drude model, but with different ϵ_1 and ϵ_2. More specifically, the

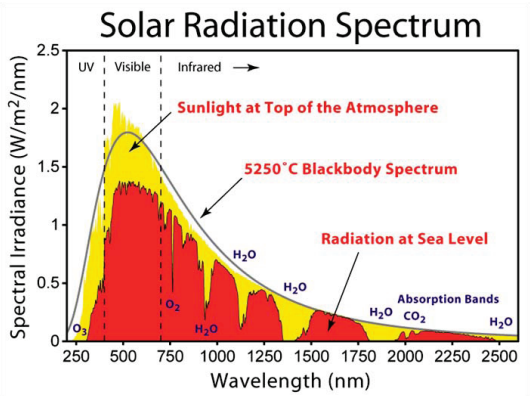

Figure 6: The solar radiation spectrum corresponding to various wavelengths: `http://en.wikipedia.org/wiki/File:Solar_Spectrum.eps`.

following ϵ_1 and ϵ_2 are used for Cu, Ni and tungsten, respectively:

$$\epsilon_1 = 100 * (390\lambda^6 - 1600\lambda^5 + 2800\lambda^4 - 2600\lambda^3 + 1300\lambda^2 - 330\lambda + 36),$$
$$\epsilon_2 = 100 * (-210\lambda^6 + 950\lambda^5 - 1800\lambda^4 + 1700\lambda^3 - 950\lambda^2 + 270\lambda - 31),$$
$$\epsilon_1 = 4.5\lambda^3 - 30\lambda^2 + 23\lambda - 15,$$
$$\epsilon_2 = -2.5\lambda^3 + 13\lambda^2 + 12\lambda + 5.3,$$
$$\epsilon_1 = 35\lambda^4 - 260\lambda^3 + 630\lambda^2 - 680\lambda + 270,$$
$$\epsilon_2 = -26\lambda^4 + 220\lambda^3 - 650\lambda^2 + 820\lambda - 340.$$

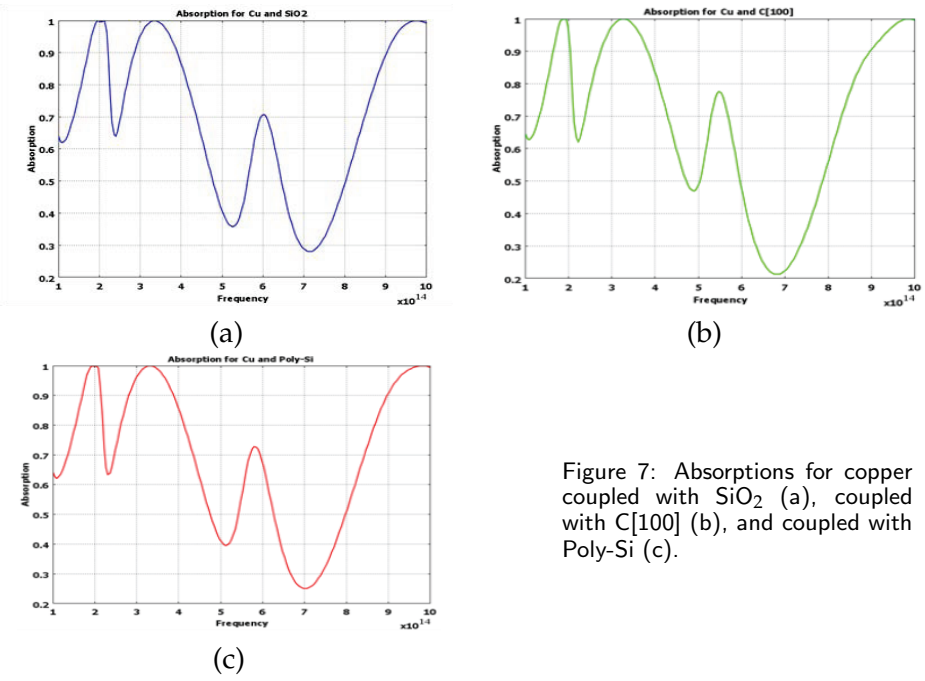

Figure 7: Absorptions for copper coupled with SiO_2 (a), coupled with C[100] (b), and coupled with Poly-Si (c).

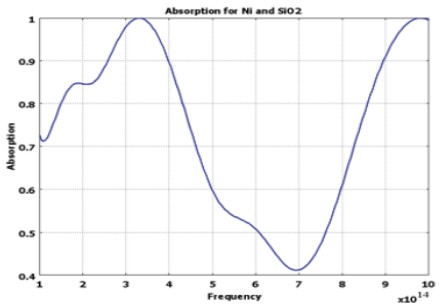

(a)

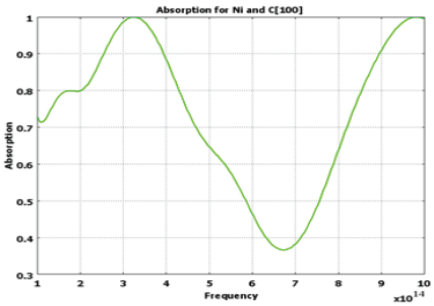

(b)

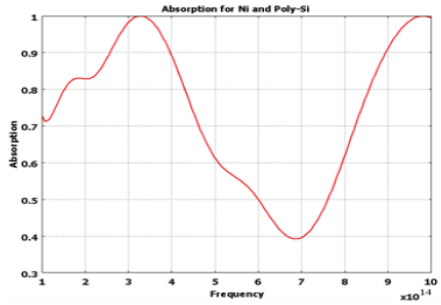

(c)

Figure 8: Absorptions for nickel coupled with SiO_2 (a), coupled with C[100] (b), and coupled with Poly-Si (c).

Results corresponding to different combinations are listed below. For simplicity, we only plotted the absorption obtained at zero incident angle for each case.

Case 3.1 (Replacing gold by copper)**.** The absorptions obtained at zero incident angle for copper in different cases are plotted in Fig. 7.

Our tests show that the best absorption is obtained in the infrared and the ultraviolet region, while the visible region does not yield a good absorption. The average absorption over the whole wave band is more than 70%, though the average absorption over the visible band is about 50%.

Case 3.2 (Replacing gold by nickel)**.** The absorptions obtained at zero incident angle for nickel in different cases are plotted in Fig. 8.

Our results show that the best absorption is obtained in the infrared and the ultraviolet region, and the average absorption over the whole wave band is more than 70%, though the average absorption over the visible band is about 50%.

Case 3.3 (Replacing gold by tungsten)**.** The absorptions obtained at zero incident angle for tungsten in different cases are plotted in Fig. 9.

Our results show that the best absorption is also obtained in the infrared and the ultraviolet region, and the average absorption over the whole wave band is more than 70%, though the average absorption over the visible band is about 55%.

From the above comparisons, we see that the absorptions are quite similar for all cases. Since Ni has the cheapest price among those three metals, so in the rest simulations, we just show results using Ni and Poly-Si combination.

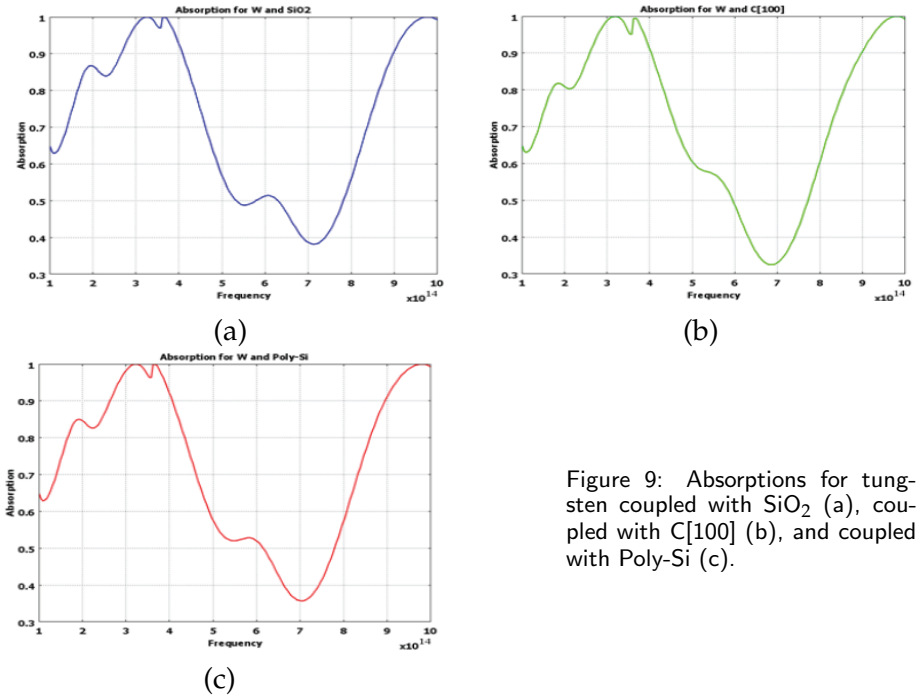

Figure 9: Absorptions for tungsten coupled with SiO_2 (a), coupled with C[100] (b), and coupled with Poly-Si (c).

3.3 Tests of other geometry designs

Now we consider how different geometry designs will affect the absorption of the solar cell. To minimize the usage of Ni, we tried to replace the metallic strip by different micro-structures.

Case 3.4 (Replacing the strip by rectangular micro-structures)**.** The first micro-structure consists of 86 equal squares arranged in three straight lines. The dimension of each square is 5×10^{-9}m by 5×10^{-9}m, which leads to a total area of Ni to be 2.15×10^{-15}m^2. In this case, the total area of Ni is less than half of the strip case, which has a total area of 4.608×10^{-15}m^2. The computed absorption and power flow are presented in Fig. 10.

Then we consided a micro-structure consisting of 44 equal rectangles, and the dimension of each square is 5×10^{-9}m by 1×10^{-8}m. The computed absorption and power flow for this structure are presented in Fig. 11.

The last micro-structure consists of 29 equal rectangles, and the dimension of each square is 5×10^{-9}m by 1.5×10^{-8}m. The computed absorption and power flow for this structure are presented in Fig. 12.

Case 3.5 (Replacing the strip by circular micro-structures)**.** We also considered the micro-structures formed by circles. The first micro-structure consists of 44 equal circles with radius 5×10^{-9}m, which leads to a total area of Ni to be 3.46×10^{-15}m^2. In this case, the total area of Ni is a little larger than half of the strip case which has a total area of 4.608×10^{-15}m^2. The computed absorption and power flow are presented in

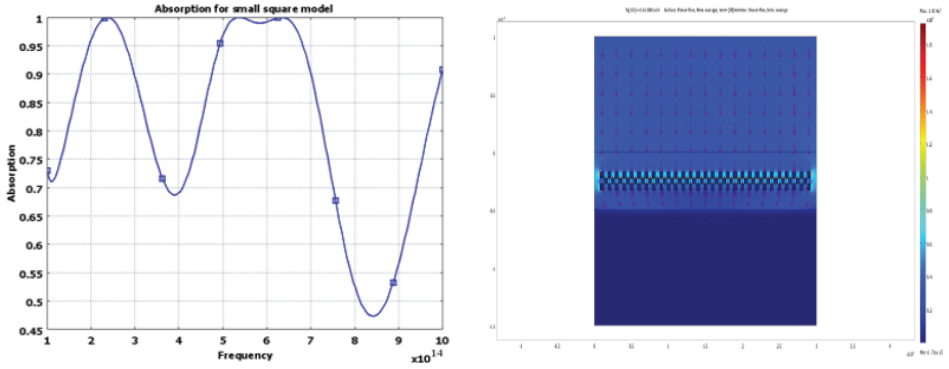

(a) (b)

Figure 10: The first rectangular micro-structure case: The absorption (a); The power flow (b).

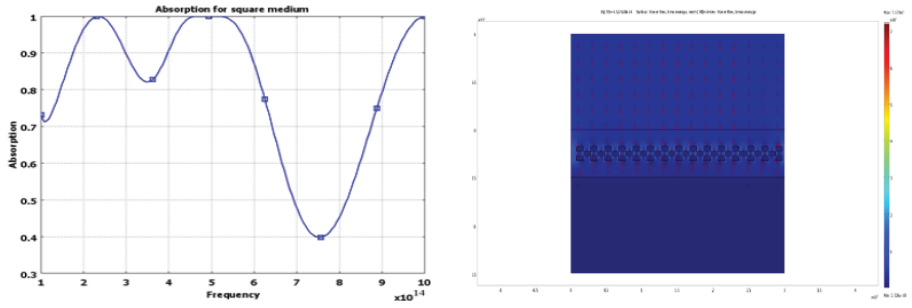

(a) (b)

Figure 11: The second rectangular micro-structure case: The absorption (a); The power flow (b).

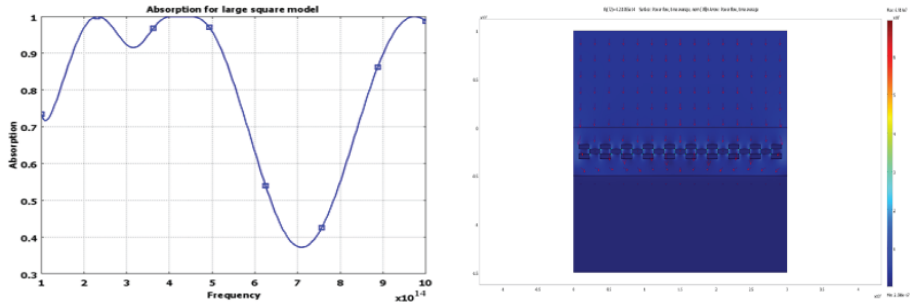

(a) (b)

Figure 12: The third rectangular micro-structure case: The absorption (a); The power flow (b).

Fig. 13.

Then we consided a micro-structure consisting of 30 equal circles with the same radius as the 44 circle case. The computed absorption and power flow for this structure are presented in Fig. 14.

The last micro-structure consists of 23 equal circles with the same radius as the 44 circle case. The computed absorption and power flow for this structure are presented in Fig. 15.

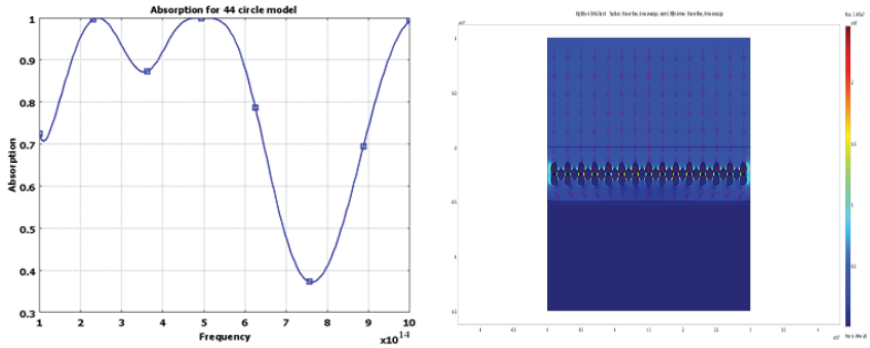

(a) (b)

Figure 13: The micro-structure formed by 44 circles: The absorption (a); The power flow (b).

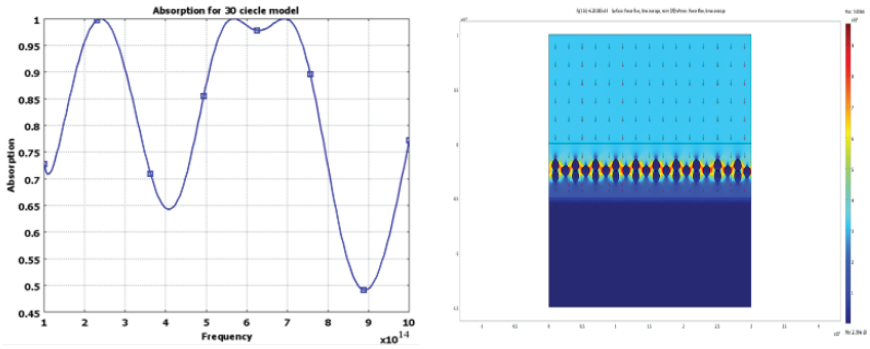

(a) (b)

Figure 14: The micro-structure formed by 30 circles: The absorption (a); The power flow (b).

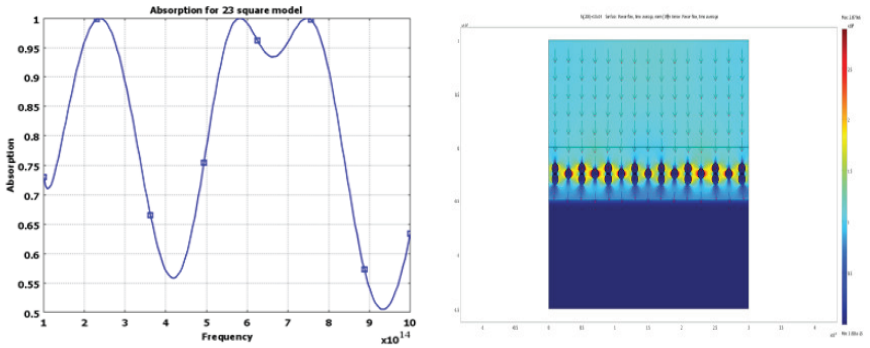

(a) (b)

Figure 15: The micro-structure with 23 circle case: The absorption (a); The power flow (b).

We summarized the above six micro-structure cases in Table 1, which shows that among the three circle micro-structures, the 30 circle case has the best absorption at 90.5% in the visible region, and 81.0% absorption for the entire solar spectrum. Among the three rectangular micro-structures, the small square case has the best absorption

at 91.3% in the visible region, and 80.9% absorption for the entire solar spectrum.

Table 1: The absorption obtained for various cases.

	Small square	Medium square	Large square	44 circles	30 circles	23 circles
Solar spectrum	80.9%	80.3%	79.7%	79.6%	81.0%	80.5%
Visible region	91.3%	80.9%	70.6%	81.0%	90.5%	85.9%

4 Concluding remarks

In this paper, we proposed several solar cell designs based on metamaterials. Extensive numerical simulations of various designs with different materials are carried out. Our tests show that metamaterial solar cells are quite efficient, and over 80% and 90% absorption rates can be attained for solar spectrum and visible rays, respectively.

Acknowledgments

This work was partially supported by the NSFC Key Project 11031006 and National Science Foundation grant DMS-0810896.

References

[1] Y. AVITZOUR, Y. A. URZHUMOV AND G. SHVETS, *Wide-angle infrared absorber based on negative index plasmonic metamaterial*, arXiv Phys. Opt., 0807 (2008), pp. 1312v1.

[2] T. J. COUTTS, *A review of progress in thermophotovoltaic generation of electricity*, Renew. Sust. Energ. Rev., 3 (1999), pp. 77–184.

[3] G. DOLLING, C. ENKRICH, M. WEGENER, C. M. SOUKOULIS AND S. LINDEN, *Simultaneous negative phase and group velocity of light in a metamaterial*, Science, 312 (2006), pp. 892–894.

[4] Y. HUANG AND J. LI, *Recent advances in time-domain Maxwell's equations in metamaterials*, in HPCA 2009 (eds. by W. Zhang et al.), Lect. Notes Comput. Sci., 5938 (2010), pp. 48–57.

[5] M. LAROCHE, R. CARMINATI AND J.-J. GREFFET, *Near-field thermophotovoltaic energy conversion*, J. Appl. Phys., 100 (2006), pp. 063704.

[6] J. LI, Y. CHEN AND V. ELANDER, *Mathematical and numerical study of wave propagation in negative-index materials*, Comput. Methods Appl. Mech. Eng., 197 (2008), pp. 3976–3987.

[7] J. LI AND A. WOOD, *Finite element analysis for wave propagation in double negative metamaterials*, J. Sci. Comput., 32 (2007), pp. 263–286.

[8] D. R. SMITH, W. J. PADILLA, D. C. VIER, S. C. NEMAT-NASSER AND S. SCHULTZ, *Composite medium with simultaneously negative permeability and permittivity*, Phys. Rev. Lett., 84 (2000), pp. 4184–4187.

[9] K. TVINGSTEDT, N.-K. PERSSON, O. INGANÄS, A. RAHACHOU AND I. V. ZOZOULENKO, *Surface plasmon increase absorption in polymer photovoltaic cells*, Appl. Phys. Lett., 91(11) (2007), pp. 113514.

[10] V. G. VESELAGO, *The electrodynamics of substances with simultaneously negative values of ϵ and μ*, Sov. Phys. Uspekhi, 47 (1968), pp. 509–514.

[11] C. WU, Y. AVITZOUR AND G. SHVETS, *Ultra-thin, wide-angle perfect absorber for infrared frequencies*, in: Metamaterials: Fundamentals and Applications (eds. by Mikhail A. Noginov, Nikolay I. Zheludev, Allan D. Boardman, Nader Engheta), Proc. SPIE, 7029 (2008), pp. 70290W.